Linking carbon nanostructure, optical properties, volume fraction, and size distribution of carbon nanoparticles formed in premixed flames

M. Bauer[1,†], F.P. Hagen[1,2,†,*], D. Kretzler[1,†], S. Schulz[1,2], B. Stelzner[1], H. Bockhorn[1], R. Suntz[2] and D. Trimis[1]

*fabian.hagen@kit.edu
† These authors contributed equally

[1] *Karlsruhe Institute of Technology (KIT), Engler-Bunte-Institute, Combustion Technology, Engler-Bunte-Ring 7, 76131 Karlsruhe*

[2] *Karlsruhe Institute of Technology (KIT), Institute of Chemical Technology and Polymer Chemistry, Engesserstraße 20, 76131 Karlsruhe*

Abstract
In this work the structure of carbon nanoparticles (CNPs) as it evolves during their formation in sooty flat premixed flames of ethylene/air stabilized on a McKenna burner at three different equivalence ratios is investigated. The question addressed is whether there is a correlation between equivalence ratios, optical particle properties, and the structural levels of CNPs. By combining two-color time-resolved laser-induced incandescence (2C-TiRe-LII) at three excitation wavelengths, 2C planar LII (2C-PLII), tunable diode laser absorption spectroscopy (TDLAS), and intrusive particle sampling coupled with differential mobility sizing (PS-DMS), the structural evolution of particles over the height above burner (*HAB*) is investigated. The parameters analyzed include the soot volume fraction f_V, the flame temperature *T*, the size distributions of aggregates $P(d_G)$, and primary particles $P(d_P)$, as well as the size of graphene-like layers of statistically distributed length $P(L_f)$ within CNPs. The results indicate a correlation between the volume fraction of the particles formed, their primary particle size, and their optical properties, and, hence, the nanostructure of the CNPs. As equivalence ratio and volume fraction increases, CNPs slightly grow in size. This is associated with a red shift in the absorption spectrum of the particles, which is due to an increase of the extension of graphene like structural units towards a more graphitic internal structure and is manifested in a decrease of the Ångström coefficient.

1. Introduction

Carbon particles - world wide production scale >13 Mt/a [1] - are employed in a variety of fields of application as functional- or electro-materials [2]. The properties essential for the application of carbon particles in the various fields are defined by their structure on different size scales. While the meso- and microstructure relate to the size distributions of primary particle aggregates $P(d_G)$ and primary particles $P(d_P)$, respectively, the carbon nanostructure defines the molecular structure. On the molecular scale carbon particles are composed of graphene-like layers as basic structural units (BSUs) with statistically distributed extension $P(L_f)$. This work addresses the structure of carbon particles as it evolves during their formation on different scales in sooty premixed hydrocarbon flames.

The understanding of the evolution of the structure of carbon particles on the meso-, micro-, and nanoscale during particle formation provides the opportunity for targeted synthesis of particles with tailored topologies. Also, structure-associated particle properties relevant for practical applications may already be controlled by the synthesis conditions. In this context, electrical conductivity for use in sensors [2], fuel cells or solar modules or reactivity against oxidation, a decisive quantity for oxidation of particles on particulate filters, can be mentioned [3].

The structural transformation of carbon particles formed in slightly sooty laminar premixed flames of ethylene/air at three equivalence ratios is investigated in this work by combining two-color time-resolved laser-induced incandescence (**2C-TiRe-LII**) using three excitation wavelengths, two-color planar LII (**2C-PLII**), tunable diode laser absorption spectroscopy (**TDLAS**) and intrusive particle

sampling coupled with differential mobility sizing (**PS-DMS**). The combination of the multiple diagnostics allows addressing the question whether soot volume fractions, properties on the meso-, micro-, and nanoscale, and optical properties are correlated. If correlations between these properties, e.g., soot volume fraction f_V, statistical characteristics of $P(d_G)$, $P(d_P)$ and $P(L_f)$, exist, access to a property allows other properties to be evaluated.

2. Experimental approach

The quantities measured in this study in laminar premixed flames of ethylene/air near the soot limit and the corresponding diagnostic techniques used for the measurements are as listed in the following:

- Gas phase temperature T: TDLAS,
- Soot volume fraction f_V: 2C-PLII, 2C-TiRe-LII, PS-DMS,
- Soot primary particles sizes and size distributions $P(d_P)$: 2C-TiRe-LII,
- Particle aggregates and size distributions $P(d_G)$: PS-DMS,
- Refractive-index function for absorption $E(m,\lambda^j_{exc})$: 2C-PLII,
- Ratio of refractive-index function for absorption at two excitation wavelengths $E(m,\lambda^i_{exc})/E(m,\lambda^j_{exc})$: 2C-TiRe-LII.

The profiles of these quantities were recorded along the height above the burner (*HAB*) in flat premixed flames of ethylene/air at different equivalent ratios Φ. Note that f_V is determined by different methods and some methods are applied for different properties. This allows mutual validation of the obtained results. In the following, the experimental setup, the measurement methods used, the measured quantities and other parameters derived from them are explained.

2.1. Laminar premixed flat flames

The experiments were performed on sooty flat premixed flames of ethylene/air stabilized on a 60 mm diameter oil-cooled McKenna porous stainless-steel burner. The total gas flow rate was kept constant at 10 slpm with an exit velocity of 6.37 cm s^{-1}. The flames were stabilized by a 60 mm stainless-steel disc mounted 20 mm above the burner surface. A total of three ethylene/air premixed flat flames at equivalence ratios near the soot limit (Φ = 2.0, 2.1 and 2.3) were investigated.

2.2. Temperature determination

Comparable to [4,5], gas phase temperatures of the investigated laminar premixed flames have been measured by **TDLAS**. A multiline thermometry approach based on a Boltzmann plot analysis using the information from seven different absorption lines is used to quantify the temperature. Two different distributed-feedback (DFB) diode lasers with central wavelengths λ = 1344.5 nm and 1392.3 nm are used for this purpose [5]. The experimental setup, selection of suitable absorption lines, characterization of the diode laser, data analysis, and determination of experimental uncertainties for the temperature and water concentration measurements are described in detail in [4]. Uncertainties in the measured temperatures of about 50 K to 100 K are obtained [6].

2.3. Determination of particle size distributions $P(d_G)$ and $P(d_P)$

Both the distribution of diameters of gyration of aggregates $P(d_G)$ and of primary particles $P(d_P)$ are measured by different methods, i.e., 2C-TiRe-LII and particle sampling coupled with differential mobility sizing, respectively.

The non-intrusive **2C-TiRe-LII** involves heating soot particles with a nanosecond laser pulse and collecting the resulting blackbody radiation. The LII signal decay is numerically computed with an energy balance equation for the laser pulse heated particles. $P(d_P)$ is computed by a multidimensional non-linear fit of the calculated to the measured LII signals. By assuming a log-normal size distribution, we apply the Karlsruhe model to compute statistical characteristics of $P(d_P)$. Details, equations, and assumptions of this model are provided in [3]. The particle temperature after laser heating is determined experimentally by the 2C method, employing Planck's radiation law. Details regarding this approach are provided in [3, 7]. In the experiments, the fundamental wavelength of a 10 Hz pulsed Nd:YAG laser at 1064 nm has been used. A half-wave plate and a polarizing beam splitter are used to provide a constant and defined energy density of the laser pulses within the low-fluence regime, i.e., fluence F lower than 0.2 J cm^{-2}, to avoid particle evaporation. The signals were collected perpendicular to the laser beam

using a lens system and two fast photomultipliers equipped with band-pass filters centered at 450 nm and 650 nm, respectively. Details of the 2C detection optics, detectors, instrumentation, mirror array, and Nd:YAG laser used are described elsewhere [3,8].

Particle sampling and differential mobility sizing (PS-DMS) enables the determination of the mobility size distribution $P(d_m)$ of particle ensembles at different HABs of the premixed flames. $P(d_m)$ represents the superposition of $P(d_P)$ and $P(d_G)$, since apart from single primary particles also fractal-like aggregates formed by coagulation are measured. Considering the primary particle size distribution $P(d_P)$ derived via 2C-TiRe-LII, conclusions about the size and number concentration of fractal-like aggregates and statistical characteristics of $P(d_G)$ can be drawn from $P(d_m)$.

To determine the mobility size distribution, we used a hole-in-tube sampling system similar to the one described by Zhao et al. [9]. A ceramic tube with an inner diameter of 9 mm and an orifice of 300 µm was placed horizontally above the burner plate and 30 slpm N_2 was flowed through. The resulting dilution ratio (*DR*) of the particle-laden flame gas sample was $DR > 10^4$. Details of the aerosol sampling system and a description of the methods used to determine and control *DR* may be found in [10]. A method applied for correcting $P(d_m)$ for particle losses in the probe and tubes is provided in [8]. For differential mobility sizing, we used an electrostatic classifier (EC), a soft X-ray neutralizer, a nano-differential mobility analyzer (nano-DMA), and a condensation particle counter (CPC). The EC was operated at a sheath flow rate of 15 slpm, while the CPC was operated at 1.5 slpm. Details of the instrumentation can be found in [8]. Frenzel et al. [10] report an unavoidable measurement uncertainty for PS-DMS of < 24 %.

2.4. Estimating the extension L_f of BSUs via optical particle properties

Williams et al. [11] suggested an influence of order, extension, and orientation of BSUs on the optical properties of nano-sized carbonaceous particles (CNPs). This hypothesis was tested in [3, 12, 13], deriving quantitative relations between statistical characteristics (e.g. mean, ninth decile etc.) of the size distributions $P(L_f)$ of BSUs and the refractive-index function for absorption $E(m,\lambda)$, with large-sized BSUs being linked to an increasing $E(m,\lambda)$ in the near-infrared spectral (NIR) range and *vice versa*. With an increasing size of the graphene-like layers the energy gap between the highest occupied molecular orbital (HOMO) and the lowest unoccupied molecular orbital (LUMO) decreases leading to increasing probability of low-energy photon absorption. The absorption spectra of CNP then exhibit a red shift with increasing extension of the BSUs [3]. The dispersive wavelength dependence of $E(m,\lambda)$ can be approximated by [14]:

$$E(m,\lambda) = \frac{\beta\,\lambda^{1-\xi}}{6\,\pi}, \tag{1}$$

with β as a scaling factor and the Ångström coefficient ξ. In a number of studies, e.g. [15, 16], decreasing Ångström coefficients have been associated with the maturity level of CNPs. In [3], we suggest that decreasing ξ are related to increasing BSU sizes.

In this study, two methods were applied allowing the determination of $E(m,\lambda_{exc})$ at three discrete wavelengths, i.e., λ_{exc} = 266 nm, 532 nm and 1064 nm. By fitting Eq. (1) to $E(m,\lambda_{exc})$ over wavelength, the Ångström coefficient can also be computed. Both $E(m,\lambda_{exc})$and ξ enable the estimation of statistical characteristics of the size distributions $P(L_f)$ of BSUs embedded within primary particles [3].

The first method is the two-color planar LII (**2C-PLII**)**.** By measuring the temperature before and after laser pulse heating of CNPs, $E(m,1064\ nm)$ can be computed according to Eq. (2) [6,17]:

$$E(m,1064\ \text{nm}) \cong \frac{1064\ \text{nm}\,\rho}{6\,\pi\,F}\int_{T_0}^{T_{LII}} c_p(T)dT. \tag{2}$$

Here, T_0 is the temperature of the particles in the flame, which was determined as explained in sec. 2.2, and T_{LII} is the temperature after laser pulse absorption. Furthermore, F is the fluence of the laser pulse, c_p is the temperature-dependent heat capacity of the particles estimated according to [18], ρ is the density of CNPs [19]. The excitation wavelength is fixed at 1064 nm in the 2C-PLII experiments, hence, the field of $E(m,1064\ \text{nm})$ can be computed by application of Eq. (2). For excitation of the 2C-PLII signal, the fundamental wavelength of a pulsed Nd:YAG laser at 1064 nm has been used. The laser beam is

shaped in a sheet optics combining three lenses with focal points of $f = -20$ mm, 500 mm and 700 mm. Beam profiling and fluence measurement are explained elsewhere [12]. Applying Planck's radiation law, the temperature of CNPs after laser pulse energy absorption T_{LII} is determined via 2D-2C pyrometry. This approach uses an image doubler to split the imaged object into two wavelengths and image them on the intensified CMOS camera. First, photons to be imaged are collected by an achromatic lens ($f = 25$ mm), parallelized and separated by a dichroic mirror with a cut-on wavelength of 615 nm. Second, the separated light beams pass each through a bandpass filter with central wavelengths of 532 nm and 656 nm. The optical setup and a detailed description of the post-processing of 2C frames and temperature analysis are given elsewhere [6]. Uncertainties in temperatures of less than 100 K are obtained [6].

As second method we used **2C-TiRe-LII** described in sec. 2.3 at three excitation wavelengths, i.e., λ_{exc} = 266 nm, 532 nm and 1064 nm. The energy absorbed from the particle ensemble heated by a laser pulse is given by [20]:

$$\dot{Q}_{abs} = \frac{\pi^2 \, d_p^3 \, E(m,\lambda_{exc}) \, F}{\lambda_{exc}}. \tag{3}$$

The left-hand side of Eq. (3) describes the absorbed laser energy of the laser pulse with the laser fluence F at λ_{exc} causing heating of the particle ensemble from T_0 *to* T_{LII}. If the particle is heated after cooling again with a second laser pulse of different excitation wavelength and accommodated laser fluence, thereby achieving coincidence of both 2C-TiRe-LII peak signals, the absorbed energies and, therefore, T_{LII} resulting from the two consecutive laser pulses are equal [3,12]. Consequently, the ratio of the refractive-index functions for absorption at the two excitation laser wavelengths can be determined from the required fluences according to Eq. (4) [3, 12, 13, 21]:

$$\frac{E(m,\lambda^i_{exc})}{E(m,\lambda^j_{exc})} = \frac{\lambda^i_{exc}}{\lambda^j_{exc}} \, \frac{F_j}{F_i}. \tag{4}$$

In this study, $E(m,266\text{ nm})/E(m,1064\text{ nm})$ and $E(m,532\text{ nm})/E(m,1064\text{ nm})$ were determined. Considering $E(m,1064\text{ nm})$ from the 2C-PLII experiments according to Eq. (2), the absolute values of $E(m,532\text{ nm})$ and $E(m,266\text{ nm})$ can be calculated. Fitting Eq. (1) to the three $E(m,\lambda)$ yields the Ångström coefficient ξ. In the following, the absolute value of $E(m,1064\text{ nm})$ and the Ångström coefficient ξ are used to analyze and discuss the experimental results.

Details of the optical setup, pulse laser, mirror array, automated matching mode method to achieve coincidence of the 2C-TiRe-LII signals, and the data analysis are described in [21]. The 2C-detection optics is explained in sec. 2.3.

2.5. Determination of soot volume fraction f_V

The soot volume fraction f_V along *HAB* is quantified using the methods applied to determine size distributions, i.e., **2C-TiRe-LII** and **PS-DMS**, see previous section. In addition, the two-dimensional field of f_V is measured via **2C-PLII**.

First, f_V can be determined from **PS-DMS** by integrating the detected $P(d_m)$ over mobility diameters. Considering the count median diameters (*CMDs*) of $P(d_P)$ derived from 2C-TiRe-LII, f_V may be computed from $P(d_m)$ using the correlations of Kelesidis and Pratsinis [22].

According to [7,8], the intensity of the **2C-TiRe-LII** signals depends on the soot volume fraction. Calibration of the laser pulse absorption signal enables the determination of f_V. Details of the calibration procedure are given in [8].

Similarly, the quantification of the volume fraction via **2C-PLII** is based on the approximate linear dependence of f_V on the intensity of the detected 2C-PLII signals. Details on the detection optics, required image processing and analysis, and calibration of the diagnostics are given in the previous section as well as in [6].

3. Results and discussion

Figure 1 shows the profiles of the soot volume fraction f_v along *HAB* and for three different equivalence ratios of Φ = 2.0, 2.1, and 2.3 determined by three different methods, i.e., 2C-TiRe-LII, PS-DMS, and 2C-PLII. The volume fractions measured with the different techniques exhibit very good agreement for

all equivalence ratios and *HABs* studied. The increase of f_V with *HAB* is approximately parabolic. Soot volume fractions f_V - not attaining their plateau values familiar from premixed sooty flames at the *HAB* measured - also increase with increasing equivalence ratio Φ. The evolution of the gas phase temperature *T* measured with TDLAS is given in Fig. 2. The temperatures increase with decreasing Φ and decrease with *HAB* in accordance with literature, e.g., ref. [6].

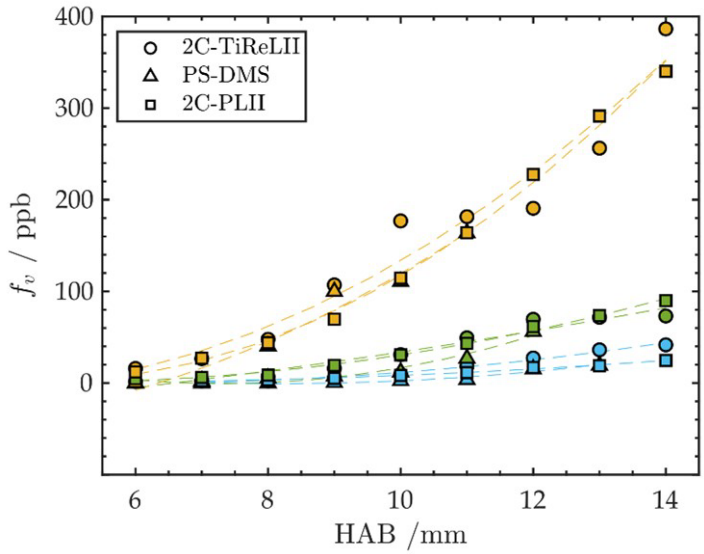

Fig. 1 Soot volume fractions f_v for the studied flat premixed flames of ethylene/air with Φ = 2.0, blue, Φ = 2.1, green, and Φ = 2.3, yellow, measured with three different methods along *HAB*. Due to possible probe clogging, determination of f_V > 200 ppb via PS-DMS was not possible.

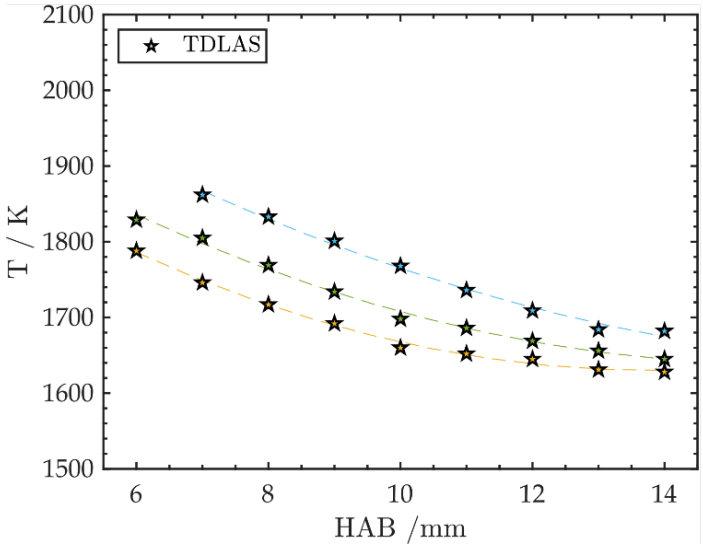

Fig. 2 Gas phase temperatures for the studied flat premixed flames of ethylene/air with Φ = 2.0, blue, Φ = 2.1, green, and Φ = 2.3, yellow, measured via TDLAS along *HAB*.

Figure 3 compares the evolution of the CMDs of the size distributions $P(d_P)$ of the primary particles and the mobility size distributions $P(d_m)$ derived using 2C-TiRe-LII and PS-DMS, respectively, along *HAB* for the three investigated equivalence ratios.

The *CMD* of the primary particle size distribution determined via 2C-TiReLII increases gradually approximately linear starting for *HAB* > 7 mm. Overall, this increase follows the growing soot volume fraction, see Fig. 1. According to Fig. 3, an influence of the equivalence ratio on primary particle growth is not evident. For the flames studied, surface growth causing growing primary particle sizes is likely insignificantly sensitive to the equivalence ratio for the conditions near the soot limit. Nascent particles formed at *HAB* < 7 mm exhibit reduced absorption at a laser excitation wavelength of 1064 nm. This

impedes the analysis of the primary particle sizes at *HAB* < 7 mm [8], while simultaneously suggesting that these particles are composed of small-sized BSUs [21], cf. below discussion.

The *CMDs* determined via PS-DMS represent the median of the mobility size distribution, which maps the volume equivalent diameter of both the primary particles and the fractal-like aggregates. For an equivalence ratio of 2.0, the *CMD* of $P(d_m)$ differs only slightly from that of $P(d_p)$, indicating that coagulation of primary particles to larger aggregates is of minor importance. Coagulation of the primary particles and hence formation of fractal-like aggregates is evident for $\Phi \geq 2.1$, as the *CMD* of $P(d_m)$ exceeds the primary particle size in the late particle formation phase at *HAB* > 10 mm. By increasing the equivalence ratio, this effect is already observed at *HAB* > 8 mm. Aggregate formation is initiated at a lower *HAB* due to the high particle number densities, which can be estimated based on the large volume fractions in combination with constant primary particle sizes. However, aggregate formation and thereby the *CMDs* of $P(d_m)$ are mainly correlated to f_V and scarcely to the *CMDs* of $P(d_P)$.

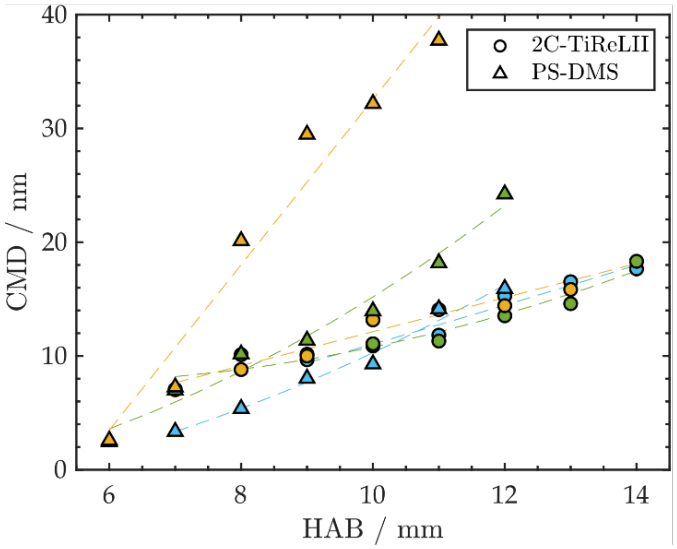

Fig. 3 Count median diameters *CMDs* of $P(d_p)$, circles, and $P(d_m)$, triangles, measured via 2C-TiRe-LII and PS-DMS, respectively, for flat premixed flames of ethylene/air with Φ = 2.0, blue, Φ = 2.1, green and Φ = 2.3, yellow, as function of *HAB*.

Figure 4 shows the refractive-index function for absorption at 1064 nm determined by 2C-PLII as a function of the equivalence ratio Φ and *HAB*. It is evident that *E(m,1064* nm*)* increases approximately linear with increasing Φ as well as with increasing *HAB*. This change in the absorption behaviour of CNPs in the near-infrared is a result of the evolution of the nanostructure of the primary particles. With increasing degree of graphitization, i.e. increasing BSU sizes, the optical band gap decreases, resulting in a red shift of the absorption spectrum, i.e. increasing *E(m,1064* nm*)* [3].

The relationship between Φ and *E(m,1064* nm*)* illustrated in Fig. 4 is likely due to changing precursor chemistry [21]. As Φ increases, the concentration of large-sized aromatic soot precursors increases [21]. This increase has a negligible effect on the primary particle size, as shown in Fig. 3, but a significant effect on carbon nanostructure of CNPs. An increased concentration of large polycyclic aromatic hydrocarbons (PAHs) causes the BSU size within primary particles and therefore the mean $L_{f,mean}$ of $P(L_f)$ to grow.

The observed increase of *E(m,1064* nm*)* along *HAB* might be due to the aging of the particles. With increasing *HAB*, the maturity of CNPs increases, which, according to [3, 23], is reflected in a progressive graphitization of the particles and an increase of the BSUs by annealing. The range of absolute values of *E(m,1064* nm*)* derived via 2C-PLII as given in Fig. 4 is in excellent agreement with data from literature, e.g. [23].

By combining 2C-PLII and 2C-TiRe-LII, $E(m,\lambda^i_{exc})$ is determined in this study at three different laser excitation wavelengths: 266 nm, 532 nm, and 1064 nm, cf. sec. 2.4. The determined values are given exemplarily in Fig. 5 for the flame at Φ = 2.0 and *HAB* = 12 mm. The blue curve represents a fit according to Eq. (2) resulting in a computed Ångström coefficient of ξ = 1.3. Radiation of shorter

wavelength, i.e., with higher photon energy, is stronger absorbed by the soot particles of this flame, resulting in larger values of $E(m,\lambda^{i}_{exc})$.

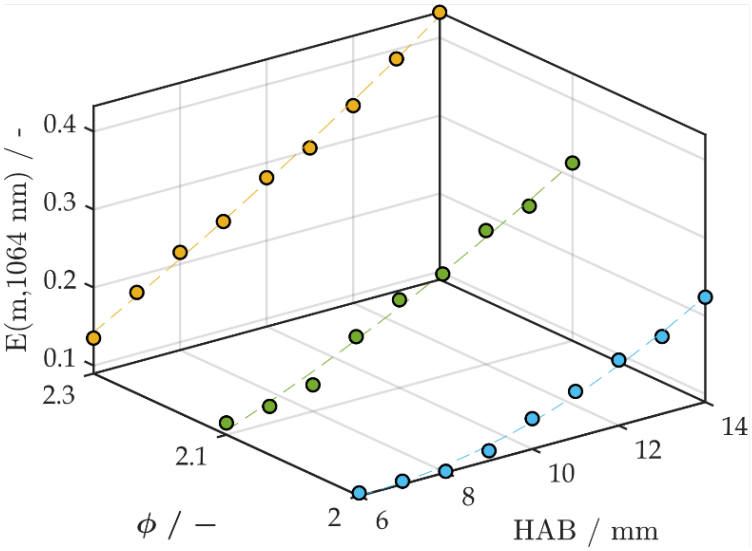

Fig. 4 Refractive-index function for absorption at 1064 nm *E(m,1064* nm*)* determined with 2C-PLII as a function of the equivalence ratio Φ and *HAB* with Φ = 2.0, blue, Φ = 2.1, green and Φ = 2.3, yellow.

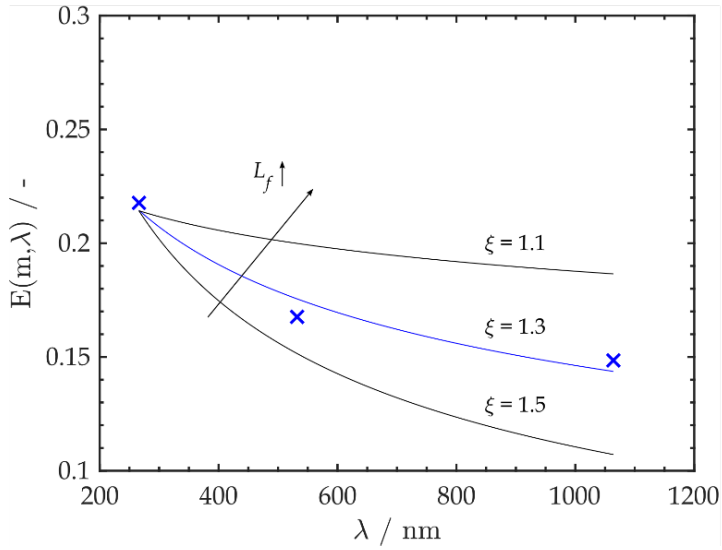

Fig. 5 Determined refractive-index function for absorption $E(m,\lambda^{i}_{exc})$ at λ_{exc} = 266 nm, 532 nm and 1064 nm, and computed fits with different Ångström coefficients. Fitting with ξ = 1.3 (blue) results in the best approximation.

The calculated values of the Ångström coefficient ξ for the total data set are given in Fig. 6, where ξ is plotted as function of Φ and *HAB*. It is obvious that with increasing equivalence ratio and increasing *HAB* the Ångström coefficient decreases, indicating an increasing absorption in the near-infrared spectral region. Thus, ξ is also a measure of the increase in the refractive-index function for absorption in the near-infrared spectral region. Decreasing Ångström coefficients indicate increasing BSU sizes within CNPs and, therefore, progressive graphitization, citing the reasons for this behavior outlined in the previous section. In addition, the computed coefficients are in very good agreement with the values proposed by Johansson et al. [15].

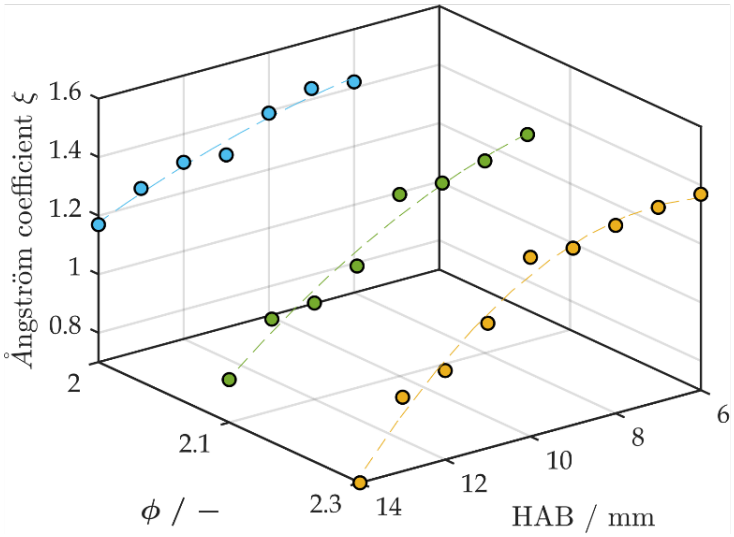

Fig. 6 Ångström coefficients ξ as a function of Φ and *HAB* with Φ = 2.0, blue, Φ = 2.1, green and Φ = 2.3, yellow.

4. Linking carbon nanostructure, optical properties, volume fraction and size distribution

Figure 7 and 8 summarize the key findings of this study. The relation of the optical properties in term of the Ångström coefficient ξ with soot volume fraction f_V and the mean primary particle sizes *CMD* for the investigated flames is displayed in Fig. 7. Figure 8 gives the mean of $P(L_f)$, based on the correlations of $E(m,\lambda)$ with $L_{f,mean}$ presented in [3] versus soot volume fractions f_V and the mean primary particle sizes *CMD*.

With increasing soot volume fraction, the absorption spectrum of the particles shifts to longer wavelengths, resulting in low Ångström coefficients. This is the result of a change in the nanostructural composition of the primary particles with increasing f_V to a more graphitic nature with large-sized BSUs embedded within primary particles, see Fig. 8.

Large soot volume fractions tend to be associated with slightly increasing *CMDs* and *vice versa*. This dependency almost disappears for small soot volume fractions, where a wide range of primary particle sizes are found. This indicates that particle size growth does not depend exclusively on the precursor concentrations determining the soot volume fraction, but also on the time available for particle formation, i.e., *HAB*. Further, increasing primary particle sizes correlate with decreasing Ångström coefficients. However, Fig. 7 also exhibits that for *CMDs* between 14 nm and 18 nm, multiple Ångström coefficients are obtained for the same primary particle size. One explanation may be found in the formation history of CNPs. Large primary particles result from soot growth at rather small equivalence ratios. At these equivalence ratios, the soot precursors present in the gas phase are small in size [21] and the nanostructure of the primary particles is determined by the growth of the BSUs occurring during particle aging along *HAB*. This results in carbon nanoparticles with moderate Ångström coefficients. Conversely, large *CMDs* can also result from fuel-rich combustion conditions at increasing Φ. Under such conditions, large aromatic clusters are already formed in the gas phase as soot precursors, which then continue to grow during the aging process. Thus, in this case, large-sized BSUs, i.e., a graphitized nanostructure, are to be expected. In Fig. 7 this is indicated by small Ångström coefficients at high soot volume fractions.

As small Ångström coefficients ξ correlate with increasing size of the BSUs [3], Fig. 8 is the mirrored picture of Fig. 7 reflecting the inverse dependence of ξ and $L_{f,mean}$. The surfaces indicated in Figs. 7 and 8 contain all data measured for the investigated flames at equivalence ratios near the soot limit. These surfaces correlate optical properties and nanostructure of soot particles formed at these conditions with soot volume fraction f_V and statistical characteristics of $P(d_P)$. The ambiguity visible in regions of larger CMDs can be traced back to the different prominence of surface growths and particle aging in the investigated flames.

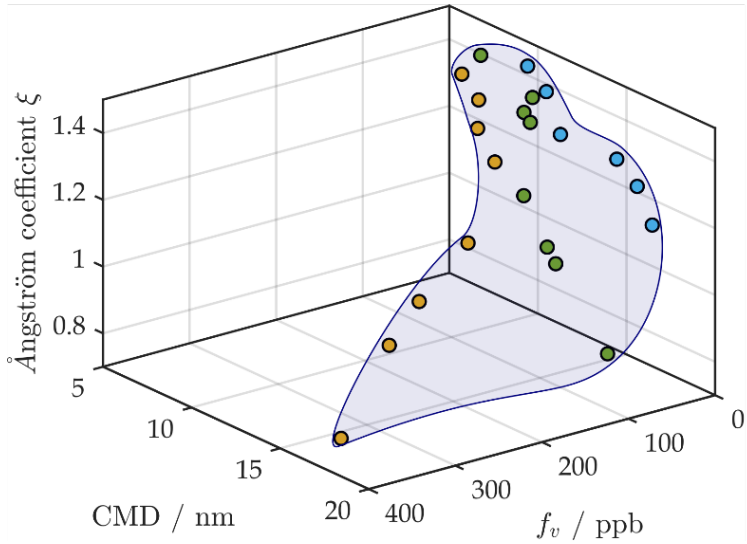

Fig. 7 Linking optical properties, volume fractions and primary particle sizes: Ångström coefficients ξ, *CMDs* of $P(d_p)$ and soot volume fractions f_v for all investigated Φ and *HAB* with Φ = 2.0, blue, Φ = 2.1, green and Φ = 2.3, yellow.

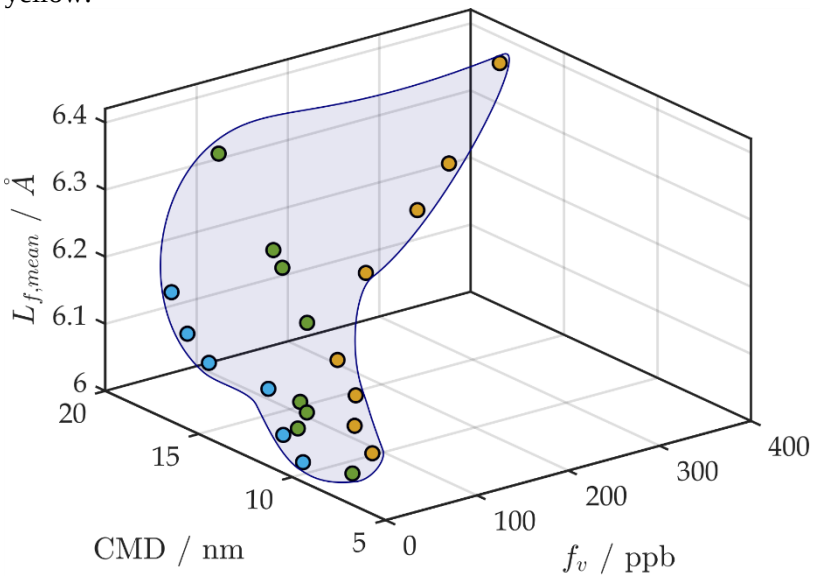

Fig. 8 Linking carbon nanostructure, volume fraction and primary particle sizes: Mean size $L_{f,mean}$ of the size distributions of BSUs $P(L_{f,mean})$, *CMDs* of $P(d_p)$ and the soot volume fractions f_v for all investigated Φ and *HAB* with Φ = 2.0, blue, Φ = 2.1, green and Φ = 2.3, yellow.

Acknowledgments

The authors kindly acknowledge the German Research Foundation (DFG) for financial support within the projects TR470/7-1/2 and SU249/6-1/2 and for funding measuring equipment within the HBFG program INST 121384/178-1 FUGG. The present research work contributes to the MTET program, Resource and Energy Efficiency, Anthropogenic Carbon Cycle (38.05.01) of Helmholtz Association.

References

[1] Singh M., Vander Wal R.L.: *Nanostructure Quantification of Carbon Blacks*, C, 5, 1-12, 2019.

[2] Grob B., Schmid J., Ivleva N.P., Niessner R.: *Conductivity for Soot Sensing: Possibilities and Limitations*, Anal. Chem., 84, 3586-3592, 2012.

[3] Hagen F.P., Kretzler D., Häber T., Bockhorn H., Suntz R., Trimis D.: *Carbon nanostructure and reactivity of soot particles from non-intrusive methods based on UV-VIS spectroscopy and time-resolved laser-induced incandescence*, Carbon, 182, 634-654, 2021.

[4] Sentko M.M., Schulz S., Stelzner B., Anderlohr C., Vicari M., Trimis D.: *Determination of temperature and water-concentration in fuel-rich oxy-fuel methane flames applying TDLAS,* Combust. Flame, 214, 336–345, 2020.

[5] von Langenthal T., Sentko M.M., Schulz S., Stelzner B., Trimis D., Zarzalis N.: *Experimental Characterization of Flame Structure and Soot Volume Fraction of Premixed Kerosene Jet* A-1 and Surrogate Flames, Appl. Sci., 11, 4796, 2021.

[6] Kretzler D., Hagen F.P., Schulz S., Bockhorn H., Suntz R., Trimis D.: *From planar laser-induced incandescence to 2D high-speed imaging of the refractive index function for absorption and volume fraction of soot,* Appl. Phys. B, 2023, submitted.

[7] Schulz C., Kock B.F., Hofmann M., Michelsen H., Will S., Bougie B., Suntz R., Smallwood G.: *Laser-induced incandescence: recent trends and current questions***,** Appl. Phys. B, 83, 333, 2006.

[8] Hagen F.P., Vlavakis P., Seitz M., Klövekorn T., Bockhorn H., Suntz R., Trimis D.: *Soot nanoparticle sizing in counterflow flames using in-situ particle sampling and differential mobility analysis verified with two-colour time-resolved laser-induced incandescence,* Proc. Combust. Inst., 39, 1119-1128, 2023.

[9] Zhao B., Yang Z., Wang J., Johnston M.V., Wang H.: *Analysis of Soot Nanoparticles in a Laminar Premixed Ethylene Flame by Scanning Mobility Particle Sizer,* Aerosol Sci. Technol., 37, 611-620, 2003.

[10] Frenzel I., Krause H., Trimis D.: *Study on the influence of ethanol and butanol addition on soot formation in iso-octane flames,* Energy Procedia, 120, 721-728, 2017.

[11] Williams T.C., Shaddix C.R., Jensen K.A., Suo-Anttila J.M.: *Measurement of the dimensionless extinction coefficient of soot within laminar diffusion flames,* Int. J. Heat Mass Transf., 50, 1616-1630, 2007.

[12] Hagen F.P., Suntz R., Bockhorn H., Trimis D.: *Dual-pulse laser-induced incandescence to quantify carbon nanostructure and related soot particle properties in transient flows – Concept and exploratory study,* Combust. Flame, 243, 112020, 2022.

[13] Hagen F.P., Kretzler D., Koch S., Bockhorn H., Suntz R., Trimis D., Kubach H., Velji A., Koch T.: *On-line monitoring of carbon nanostructure and soot reactivity in engine exhaust by dual-pulse laser-induced incandescence,* Combust. Flame, 254, 112850, 2023.

[14] Michelsen H.A.: *Understanding and predicting the temporal response of laser-induced incandescence from carbonaceous particles,* J. Chem. Phys., 118, 7012-7045, 2003.

[15] Johansson K.O., El Gabaly F., Schrader P.E., Campbell M.F., Michelsen H.A.: *Evolution of maturity levels of the particle surface and bulk during soot growth and oxidation in a flame,* Aerosol Sci. Technol., 51, 1333-1344, 2017.

[16] Bauer F.J., Braeuer P.A.B., Wilke M.W.R., Will S., Grauer S.J., *2D in situ determination of soot optical band gaps in flames using hyperspectral absorption tomography,* Combust. Flame, 112730, 2023.

[17] Török S., Mannazhi M., Bengtsson P.E.: *Laser-induced incandescence (2λ and 2C) for estimating absorption efficiency of differently matured soot,* Appl. Phys. B, 127, 96, 2021.

[18] Kock B.F., Tribalet B., Schulz C., Roth P.: *Two-color time-resolved LII applied to soot particle sizing in the cylinder of a Diesel engine,* Combust. Flame, 147, 79-92, 2006.

[19] Choi M.Y., Mulholland G.W., Hamins A., Kashiwagi T.: *Comparisons of the soot volume fraction using gravimetric and light extinction techniques,* Combust. Flame, 102, 161-169, 1995.

[20] Michelsen H.A., Schrader P. E., Goulay F.: *Wavelength and temperature dependences of the absorption and scattering cross sections of soot,* Carbon, 48, 2175-2191, 2010.

[21] Hagen F.P., Vlavakis P, Bockhorn H., Suntz R., Trimis D.: *From molecular to sub-μm scale: The interplay of precursor concentrations, primary particle size, and carbon nanostructure during soot formation in counter-flow diffusion flames,* Combust. Flame, 112729, 2023.

[22] Kelesidis G.A., Pratsinis S.E.: *Determination of the volume fraction of soot accounting for its composition and morphology,* Proc. Combust. Inst., 38, 1189-1196, 2021.

[23] Eremin A.V., Gurentsov E.V., Kolotushkin R.N.: *The change of soot refractive index function along the height of premixed ethylene/air fame and its correlation with soot structure,* Appl. Phys. B, 126, 2020.